An origin of excess vibrational entropies at grain boundaries in Al, Si and MgO: A first-principles analysis with lattice dynamics

Journal:	*Physical Chemistry Chemical Physics*
Manuscript ID	CP-ART-02-2021-000790.R1
Article Type:	Paper
Date Submitted by the Author:	29-Mar-2021
Complete List of Authors:	Yokoi, Tatsuya; Nagoya University, Department of Materials Physics Ikawa, Keiya; Nagoya University Nakamura, Atsutomo; Nagoya University, Department of Materials Physics Matsunaga, Katsuyuki; Nagoya University, Materials Physics

An origin of excess vibrational entropies at grain boundaries in Al, Si and MgO: A first-principles analysis with lattice dynamics

T. Yokoi[1,*], K. Ikawa[1], A. Nakamura[1], K. Matsunaga[1,2]

[1]Department of Materials Physics, Nagoya University, Nagoya 464-8603, Japan
[2]Nanostructures Research Laboratory, Japan Fine Ceramics Center, Nagoya, 456-8587, Japan

* Corresponding author.
E-mail address: yokoi@mp.pse.nagoya-u.ac.jp (T. Yokoi)
Phone number: +81-52-789-3365

Abstract

First-principles lattice dynamics is applied to symmetric tilt grain boundaries (GBs) in Al, Si and MgO, with the goal of revealing critical factors in determining excess vibrational entropies at the atomic level. Excess vibrational entropies at GBs are found to vary depending on the substances. Al GBs tend to show larger excess entropies and hence larger temperature dependence of the GB free energies than those in Si and MgO. Most of the Si GBs show small excess entropies. For Al and MgO, atom-projected vibrational entropies are well correlated with bond-length changes at GB cores, and have large positive values as bond lengths increase for GB atoms. This demonstrates that a similar mechanism likely dominates excess vibrational entropies of GBs for both substances, despite their dissimilar bonding nature. For Si GBs, atoms with threefold coordination do not simply follow such a correlation, implying the importance of other factors that are different from bond-length changes. These systematic comparisons will be a foothold for understanding a physical origin of excess entropies at GBs even in more complex substances.

Keywords: Ab initio calculations; Lattice dynamics; Grain boundary structure; Thermodynamic stability; Entropy

1. Introduction

For polycrystalline and nanocrystalline materials, physical properties of grain boundaries (GBs) often govern a wide variety of material properties such as mechanical properties, electrical and thermal conductivities. GB free energies are also one of the important GB properties, as they have impacts on microstructure evolution and the resultant functionalities, through affecting grain growth and solute/impurity segregation. Temperature dependence of GB free energy is a critical factor in determining thermodynamic stability of GBs, as indicated by thermal grooving measurements on metals and oxides [1-4]. Readey and Jech reported that for a symmetric tilt GB

(STGB) in NiO, its GB energy strongly decreases with increasing temperature [1]. For yttria-stabilized ZrO_2, Tsoga and Nikolopoulos showed a moderate decrease in GB free energy as temperature increased, which was comparable to that of surface energy [3]. Recently Kelly et al. reported that with increasing temperature, relative GB free energies decreased for pure Al_2O_3 while increased for doped Al_2O_3 [4]. Those studies indicate that there likely exist multiple factors in determining temperature dependence of GB free energy, and also that such factors may depend on each substance. Thus an understanding of how each factor influences GB free energy at a given temperature is essential, in order to control thermodynamic stability of polycrystalline and nanocrystalline macrostructures in a wide range of temperatures.

Among many factors, excess entropies originating from GBs are a fundamental quantity in GB thermodynamics. However, its contribution to GB free energy is still not fully understood quantitatively, due to the difficulty of experimentally determining entropic contributions in actual polycrystals. To complement this difficulty, classical atomistic simulations and density-functional-theory (DFT) calculations have become powerful tools for understanding energetics of GBs at the atomic level. Previous theoretical studies have examined connections between GB free energy on GB atomic structure as functions of their misorientation angle and rotational axis for metal [5,6], covalent [7,8] and ionic systems [9-11]. Systematic search for metastable structures has been also conducted by employing simulated annealing and evolutionary search methods based on molecular simulations [12,13], in order to understand GB-structure transitions and their properties observed experimentally at finite temperatures [14-16]. However, most theoretical studies are limited to zero-temperature GB energies, without explicit consideration of entropic contributions to GB free energies. Consequently, there is still limited knowledge about how excess entropies are generated from GB atomic structure. In particular, excess vibrational entropies, which arise from differences between lattice vibration modes of bulk and GB atoms, have been scarcely investigated although they always exist at finite temperature.

Some earlier studies employed lattice dynamics methods based on empirical interatomic potentials in order to reveal contributions of excess vibrational entropies to GB free energies [17-20]. Hashimoto et al. calculated excess vibrational entropies of STGBs in Al and indicated that a particular GB with an atom adjacent to an empty space has a larger excess entropy than that without such an atom [17]. According to a previous study by Najafabadi et al., some twist GBs in Au showed their most stable structures that are different at 0 K and 700 K, due to their excess entropy differences [18]. For a STGB in MgO, Harris et al. reported that its excess vibrational entropy is small, leading to a little decrease in GB free energy from 1.55 J/m^2 at 300 K to 1.50 J/m^2 at 1200 K [20]. These results indicate that vibrational entropies strongly depend on GB atomic structures and potentially bonding nature. However, empirical interatomic potentials often fail to accurately capture DFT potential-energy surfaces at GBs [21-23], and their accuracy may also depend on each GB structure. These facts make it difficult to compare between different GBs with respect to excess vibrational entropies. In addition, functional forms used for empirical potentials vary depending on bonding state, leading to the difficulty of quantitatively comparing excess vibrational entropies for substances with different bonding nature.

In a recent study on tungsten GBs by Scheiber et al., DFT calculations were combined with lattice dynamics based on the harmonic and quasiharmonic approximation [24]. Their DFT calculations and an analytic thermodynamic model [25] showed different values in GB free energy, demonstrating that DFT calculations are required to determine GB free energy quantitatively. Our recent work also employed the harmonic approximation based on DFT calculations in order to reveal how excess vibrational entropies are generated from GB atomic structures in MgO [26]. It was found that bond length changes of GB atoms from that of bulk atoms are well correlated with atom projected vibrational entropies, indicating that GB structures with longer bond lengths have a large excess vibrational entropy. For substances other than MgO, however, it is still unclear whether such atomic environment at GBs is also a critical factor in determining excess vibrational entropy.

With the goal of revealing critical factors in determining excess vibrational entropies of GBs for a wide range of solids, the present study systematically compares metal, covalent and ionic systems by performing DFT-based lattice dynamics. Here Al, Si and MgO are examined as model cubic systems. According to the coincidence site lattice (CSL) theory, structural characteristics of CSL-GBs can be crystallographically classified in terms of their Σ values, which are determined only from their original crystal systems. In this regard, these three materials are the same cubic system, yet have different chemical bonding states such as typical metallic, covalent, and ionic bonding. Depending on the difference in bonding nature, it can be expected that GB core structures involve specific structural units, atomic-coordination deficiency and bond lengths, as shown later. Such variations are found to be critical in determining vibrational thermodynamics of GBs. Their comparison is thus expected to provide a fundamental understanding of how bonding nature affects correlations between GB atomic structures and excess vibrational entropies, which will be a foothold to study substances with more complex bonding nature. STGBs with the [001] and $[\bar{1}10]$ tilt axes are investigated. A comparison between the most stable and metastable GB structures is also made to examine possibilities of first-order transition of GB structures at finite temperatures. Furthermore, accuracy of commonly used empirical potentials is also examined by excess vibrational entropies and phonon modes to DFT results, in order to reveal their applicability for quantitatively calculating excess vibrational entropies.

2. Computational method

2.1 DFT calculation and empirical interatomic potential

DFT calculations were performed using the projector augmented wave (PAW) method [27,28] implemented in the Vienna *Ab initio* Simulation Package (VASP) [29,30]. The exchange-correlation energy was calculated using the revised version of the generalized gradient approximation formulated by Perdew, Burke and Ernzerhof (GGA-PBEsol) [31]. Electrons $3s^2 3p^2$ for Si, $3s^2 3p^1$ for Al, $2s^2 2p^4$ for O and $3s^2$ for Mg were treated as valence electrons. Electronic wave functions were expanded using a plane-wave basis set with energy cutoffs of 320, 500 and 520 eV for Al, Si and MgO, respectively. The number of k-point meshes was set to 30 × 30 × 30, 4 × 4 × 4 and 4 × 4 × 4 for conventional cells of Al, Si and MgO, respectively. The energy convergence criterion was chosen to be 10^{-5} eV for structural relaxation in order to search for low energy structures. By changing the convergence criterion from 10^{-5} eV to 10^{-8} eV, the lowest-energy and metastable structures were again optimized and then used for lattice dynamics calculations. For structural relaxation, atomic positions were updated until the atomic forces acting on each atom became less than 10^{-2} eV/Å.

For comparison with DFT calculations, classical molecular simulations were performed using the general utility lattice program (GULP) [32]. For MgO, a Buckingham-type potential was used with a set of empirical parameters reported by Landuzzi et al. [33]. The rigid-ion model was assumed by setting formal changes of Mg and O ions to +2 and -2, respectively. For Si, the Tersoff [34] potential was used, and a modified embedded-atom-method (MEAM) potential parameterized by Lee et al. [35] was used for Al.

2.2 Lattice dynamics calculations

Lattice dynamics calculations were performed using the finite displacement method implemented in the PHONOPY code [36]. In this method, a displacement of 0.01 Å was imposed to an atom. Here the harmonic approximation was employed to calculate second-order force constants, phonon modes and thermodynamic properties. Note that the in our previous study, the quasiharmonic approximation was also applied to a Σ5(310) GB in MgO to examine the effect of thermal expansion [26]. Consequently, thermal expansion had minor effects on the excess vibrational entropy, at least at around 1000 K. This indicates that the harmonic approximation is sufficient for examining the temperature dependence of GB free energies. Although anharmonic vibration may also affect GB free energies at high temperatures as indicated by a recent study based on an empirical potential [37], such analyses with DFT calculations are still computationally very demanding. The present study is thus restricted within harmonic lattice vibration.

It was assumed that a GB free energy per unit area ΔF_{GB} is equal to an increase in Helmholtz free energy F per unit area and that the entropic contribution arises from the vibrational entropy S^{vib} alone. In this assumption, *F* is expressed as

$$F = E^{\mathrm{static}} + F^{\mathrm{vib}} = E^{\mathrm{static}} + E^{\mathrm{vib}} - TS^{\mathrm{vib}}, (1)$$

where E^{static} is the zero-temperature total energy, and E^{vib} is the vibrational internal energy. The vibrational Helmholtz free energy F^{vib} at a temperature *T* is given by

$$F^{\mathrm{vib}} = \sum_i \left[\frac{1}{2}\hbar\omega_i + k_B T \ln\left\{1 - \exp\left(-\frac{\hbar\omega_i}{k_B T}\right)\right\}\right], (2)$$

where $\hbar$ is the reduced Planck constant, k_B is the Boltzmann constant, and ω_i is the phonon frequency of the *i*th mode. The vibrational entropy S^{vib} is defined as the negative of the derivative of F^{vib} with respect to *T*:

$$S^{\mathrm{vib}} = -\frac{\partial F^{\mathrm{vib}}}{\partial T} = \frac{1}{2T}\sum_i \hbar\omega_i \coth\left(\frac{\hbar\omega_i}{2k_B T}\right) - k_B \sum_i \ln\left[2\sinh\left(\frac{\hbar\omega_i}{2k_B T}\right)\right].(3)$$

To examine the dependence of S^{vib} on atomic environments at GBs, S^{vib} was divided into the atom-projected vibrational entropy $S^{\mathrm{vib}}_{\mu,j}$ for the μth atom for the wave vector ***k*** and mode *j*, as follows:

$$S^{\mathrm{vib}}_{\mu,j} = \frac{1}{2T}\sum_i |e_i(\boldsymbol{k},j;\mu)|^2 \hbar\omega_i \coth\left(\frac{\hbar\omega_i}{2k_B T}\right) - k_B \sum_i |e_i(\boldsymbol{k},j;\mu)|^2 \hbar\omega_i \ln\left[2\sinh\left(\frac{\hbar\omega_i}{2k_B T}\right)\right], (4)$$

where $e_i(\boldsymbol{k},j;\mu)$ is the *i*th Cartesian component of a polarization vector. The atom-projected vibrational entropy for the μth atom (S^{vib}_{μ}) was then obtained by summing $S^{\mathrm{vib}}_{\mu,j}$ over 3*N* modes. ΔF_{GB} was calculated from the difference between *F* for a GB structure and the perfect-crystal cell, denoted as F_{GB} and F_{BULK}, respectively. In addition, ΔF_{GB} was separated into each term per unit area in the right side in Eq. (1):

$$\Delta F_{\mathrm{GB}} = \Delta E^{\mathrm{static}}_{\mathrm{GB}} + \Delta E^{\mathrm{vib}}_{\mathrm{GB}} - T\Delta S^{\mathrm{vib}}_{\mathrm{GB}}, (5)$$

where $\Delta E^{\mathrm{static}}_{\mathrm{GB}}$, $\Delta E^{\mathrm{vib}}_{\mathrm{GB}}$ and $\Delta S^{\mathrm{vib}}_{\mathrm{GB}}$ are the excess internal energy, the excess vibrational internal energy and excess vibrational entropy, respectively, all of which were scaled by the GB area of each GB.

2.3 Computational cell with grain boundary

Table 1 lists crystallographic properties of the GBs examined in this work. For Al, Si and MgO, eight GBs were constructed by varying misorientation angles of two grains (2θ) about the $[001]$ and $[\bar{1}10]$ tilt axes, in order to systematically examine a wide range of GB atomic structures. A GB simulation cell was built such that the *x*-axis is normal to the GB plane, the *z*-axis is oriented along the tilt axis, and the *y*-axis is oriented along the GB plane and perpendicular to the *z*-axis. The *x*-, *y*- and *z*-axis dimensions are denoted as L_x, L_y and L_z, respectively. For atoms located at the most distant position from the GB plane, the phonon partial density of states (PDOS) was found to be almost the same as that in the perfect crystal when $L_x > 13$ Å. This ensures that ΔF_{GB}

successfully converges to a constant value for L_x listed in Table 1.

To search for low-energy structures for each GB, a γ-surface method was employed in the following manner. Initially, multiple simulation cells were constructed by incrementally translating one grain relative to the other along the *y*- and *z*-axis. The length of the translation vector was set to 1 Å along each of the two axes. All simulation cells constructed were then fully relaxed, and their GB energies at 0 K were calculated. Finally, the lowest-energy and metastable structures at 0 K were used for lattice dynamics calculations. Here a "metastable" structure means that its atomic configuration after structural relaxation is different from those of the lowest-energy structure at 0 K, with higher $\Delta E_{\mathrm{GB}}^{\mathrm{static}}$ than that of the lowest-energy one. In this work, the second lowest-energy structures at 0 K were chosen as metastable structures.

In lattice dynamics calculations, supercells were constructed to account for a sufficient number of phonon modes. Thus a 2 × 2 × 2 supercell was used for Si and MgO, whereas a 3 × 3 × 3 supercell was used for Al. After structural relaxation, the GB computational cells in Table 1 were also repeated in the *y*- and *z*-axis so that L_y and L_z are larger than those of 2 × 2 × 2 and 3 × 3 × 3 supercells of the conventional cells for MgO/Si and Al, respectively.

3. Results

3.1 Lowest-energy and metastable structures

Figure 1 illustrates the lowest-energy structures obtained from the γ-surface method and used for lattice dynamics calculations. Their $\Delta E_{\mathrm{GB}}^{\mathrm{static}}$ and excess volume (ΔV) are plotted in Figs. S1 and S2 in the Supporting Information. As shown in Fig. 1, characteristic structural units (SUs) are formed depending on each of the substances. For MgO, most of the GBs studied have open structures with empty spaces at their GB cores and with mirror symmetry, as indicated by the black lines in the Σ13(510) GB. The same structures were reported in previous atomistic and DFT studies [26,38,39]. For the Σ13(320) GB, the lowest-energy structure is observed to be non-mirror symmetry. This GB structure has $\Delta E_{\mathrm{GB}}^{\mathrm{static}}$ = 1.73 J/m^2, as small as the other GBs with the [001] tilt axis, indicating a reasonably low-energy structure. A similar structure was reported in a previous atomistic simulation in NiO [40], although no previous study reported an atomic structure of the Σ13(320) GB in MgO.

For the Al GB structures, SUs are indicated by the black lines. According to the notion in previous studies [41,42], the Σ13(510) and Σ5(310) GBs contain the same SU labeled as C, and the Σ5(210) and Σ13(320) GBs contain the US named B'. The Σ9(221) and Σ3(112) GBs are non-mirror symmetry with the |E| and |DC| SU arrangements, respectively, whereas the Σ3(111) and Σ11(113) GBs are mirror symmetry with the D or C SU, respectively. These GB structures are in good agreement with those by previous atomistic studies on GBs in fcc metals [42-45].

For Si, most of the GBs consist of 4-fold-coordinated atoms without dangling bonds.

The Σ5(310), Σ9(221) and Σ13(510) GBs are non-mirror symmetry, whereas the other GBs are mirror-symmetry. These structures agree with those in the literature [46,47]. It should be noted that for the Σ3(112) GB, the globally lowest-energy structure was reported to require two repeats of the simulation cell along the $[\bar{1}10]$ tilt axis [46]. It is also noted that the Σ13(510) GB obtained corresponds to the second lowest structure close in GB energy to the lowest-energy one, according to a previous theoretical study [48]. To obtain the lowest-energy structure of the Σ13(510) GB, one would require SA-based methods [48] or more advanced search methods such as genetic algorithm [7], instead of the γ-surface method alone. However, the goal of the current work is to reveal critical factors in determining $\Delta S_{\mathrm{GB}}^{\mathrm{vib}}$, namely temperature dependence of σ_{GB}. Thus in order to systematically examine GBs in the same conditions within the γ-surface method, all the computational cells of GBs were fixed to one repeat unit along the tilt axis.

Figure 2 shows metastable structures for the Σ5(310) and Σ13(510) GBs. For the MgO GBs, the metastable structures have dense structures without empty spaces although the lowest-energy structures have the open structures (see Fig. 1). For the Al GBs, the metastable ones are non-mirror symmetry, whereas the lowest-energy atomic arrangements are mirror-symmetry with respect to the GB planes. For the metastable structures studied, their $\Delta E_{\mathrm{GB}}^{\mathrm{static}}$ values are 0.004-0.53 J/m^2 higher than those of the lowest-energy counterparts, as listed in Table S1 in the Supporting Information.

3.2 Grain boundary free energy and excess vibrational entropy

Figure 3 shows ΔF_{GB} of the individual GBs as a function of *T*. The slope of each curve is almost the same as the value of $\Delta S_{\mathrm{GB}}^{\mathrm{vib}}$, because $\Delta E_{\mathrm{GB}}^{\mathrm{vib}}$ and $\Delta S_{\mathrm{GB}}^{\mathrm{vib}}$ become nearly constant at *T* above around 100 K, and the term $-T\Delta S_{\mathrm{GB}}^{\mathrm{vib}}$ predominantly affects ΔF_{GB} with increasing *T*. This trend is observed for the three substances as shown in Fig. S3 in Supporting Information. For all GBs for Al, Si and MgO, $\Delta S_{\mathrm{GB}}^{\mathrm{vib}}$ takes positive values, and hence ΔF_{GB} decreases with increasing *T*. This trend is consistent with previous lattice dynamics calculations on GBs [17,18,24,26].

It is observed that the temperature dependences of ΔF_{GB} vary depending on GBs due to variations of $\Delta S_{\mathrm{GB}}^{\mathrm{vib}}$; ΔF_{GB} decreases by 0.065-0.38 J/m^2, 0.0071-0.085 J/m^2 and 0.0048-0.084 J/m^2 from 0 K to half of the melting point for the MgO, Al and Si GBs, respectively. Among these GBs, the Σ13(510) and Σ13(320) GBs have larger $\Delta S_{\mathrm{GB}}^{\mathrm{vib}}$ for the three substances. As a result, the Σ13 GBs show larger decreases in ΔF_{GB} with increasing *T* and become thermodynamically more stable than some GBs at finite temperatures. For example, the Σ13(320) GB in MgO (light blue curve) becomes more stable than the Σ5(310) GB at about 700 K, while the Σ13(320) GB is energetically higher at 0 K. Similarly, the Σ13(510) GB in Al (red curve) becomes more stable than the Σ9(221) GB at 380 K. For these examples, the transition temperatures are less than half of the melting points for MgO and Al, indicating that such transition of relative thermodynamic stability of GBs can occur even at moderate temperatures. Similar transitions of GB structures were also theoretically indicated in the literature [18,24,26]. Therefore, contributions of $\Delta S_{\mathrm{GB}}^{\mathrm{vib}}$ to ΔF_{GB} are physically non-negligible, and have an impact on thermodynamic stability of GBs.

Figure 3 also shows that the most stable and metastable GBs have a small but non-negligible difference in $\Delta S_{\mathrm{GB}}^{\mathrm{vib}}$ for some GBs. For the Σ3(112) GB in MgO, its metastable structure is 0.02 J/m^2 higher in $\Delta E_{\mathrm{GB}}^{\mathrm{static}}$ than the most stable one, while it becomes the most stable at about 730 K. Such transition was also reported in recent theoretical studies on STGBs in W [24] and Cu [38]. Although the current work examines only STGBs with low Σ values, first-order transition of GB structures may be a common phenomenon for various substances. It is also expected that general GBs, which likely have more complicated atomic structures than STGBs, have a diverse of metastable structures close in GB energy. Thus GB-structure transition may more frequently occur for general GBs than STGBs.

Figure 4 shows $\Delta S_{\mathrm{GB}}^{\mathrm{vib}}$ as a function of 2θ at half of melting points for MgO, Al and Si. Their comparison indicates that magnitudes of $\Delta S_{\mathrm{GB}}^{\mathrm{vib}}$ ~~depends~~ depend on the substances. MgO and Al have similar values for the $[001]$ and $[\bar{1}10]$ STGBs, although their relative values vary with the misorientation angle and tilt axis. For Si, both $[001]$ and $[\bar{1}10]$ STGBs are entirely smaller in $\Delta S_{\mathrm{GB}}^{\mathrm{vib}}$ than the MgO and Al GBs, ranging between 0.60 × 10^{-4} mJ·K^{-1}·m^{-2} and 1.04 × 10^{-4} mJ·K^{-1}·m^{-2}. Due to the small $\Delta S_{\mathrm{GB}}^{\mathrm{vib}}$ values, most of the Si GBs show less temperature dependence of ΔF_{GB}, as shown in Fig. 3(c). In Si polycrystals, GB distribution may thus be similar between 0 K and finite temperature at least for STGBs with low-Σ values. It is expected that temperature dependence of ΔF_{GB} varies with bonding nature and that covalent-bonding systems may show small $\Delta S_{\mathrm{GB}}^{\mathrm{vib}}$.

3.3 Excess vibrational entropy and GB properties

To understand critical factors in determining the magnitude of $\Delta S_{\mathrm{GB}}^{\mathrm{vib}}$, this section firstly shows correlations of $\Delta S_{\mathrm{GB}}^{\mathrm{vib}}$ with GB properties. Here the zero-temperature GB energy ($\Delta E_{\mathrm{GB}}^{\mathrm{static}}$) and excess volume per unit area of a GB plane (ΔV) are examined. ΔV is defined as the change in local volume at a GB-core region from the bulk value. Figure 5 shows the correlation between $\Delta S_{\mathrm{GB}}^{\mathrm{vib}}$ and $\Delta E_{\mathrm{GB}}^{\mathrm{static}}$ for both the lowest-energy and metastable structures. The two quantities exhibit a rough correlation, although data points are scattered and also the correlation depends on each of the tilt axes. With the assumption that $\Delta S_{\mathrm{GB}}^{\mathrm{vib}}$ linearly increases as a function of $\Delta E_{\mathrm{GB}}^{\mathrm{static}}$, the correlation factors of MgO, Al and Si are calculated to be 0.77, 0.94 and 0.82, respectively. It is thus expected that a GB with large $\Delta E_{\mathrm{GB}}^{\mathrm{static}}$ exhibits large $\Delta S_{\mathrm{GB}}^{\mathrm{vib}}$ and thereby the large temperature dependence of ΔF_{GB} for all the substances.

Figure 6 shows the correlation between $\Delta S_{\mathrm{GB}}^{\mathrm{vib}}$ and ΔV. It is found that their correlation strongly depends on each material. For MgO the data points are significantly scattered, with a correlation factor of 0.28, indicating no explicit correlation. This trend is consistent with our previous studies based on the PBE functional [26]. Similarly, the Si GBs also do not show a clear correlation between the two quantities, although GBs with smaller ΔV tend to have larger $\Delta S_{\mathrm{GB}}^{\mathrm{vib}}$. It was theoretically indicated that in MgO and Si, crystallographically more complicated STGBs and ATGBs often have SUs and coordination environments similar to the $[001]$ and $[\bar{1}10]$ STGBs [8,49]. Thus more complicated GBs in MgO and Si also may not have a strong correlation between $\Delta S_{\mathrm{GB}}^{\mathrm{vib}}$ and ΔV. On the other hand, the Al GBs show a relatively strong correlation between the two quantities, with a correlation factor of 0.90. The Al GBs studied also show a clear positive correlation between $\Delta E_{\mathrm{GB}}^{\mathrm{static}}$ and ΔV, with a correlation factor of 0.99 (see Fig. S4 in Supporting Information). For Al GBs, ΔV thus may be a critical factor in determining both $\Delta S_{\mathrm{GB}}^{\mathrm{vib}}$ and $\Delta E_{\mathrm{GB}}^{\mathrm{static}}$, and thereby ΔF_{GB}.

3.4 Excess vibrational entropy and GB atomic and electronic structures

Section 3.3 shows the correlation of $\Delta S_{\mathrm{GB}}^{\mathrm{vib}}$ with $\Delta E_{\mathrm{GB}}^{\mathrm{static}}$ and ΔV. However, the two quantities are averaged properties and thus do not provide more detailed information about generation mechanisms of $\Delta S_{\mathrm{GB}}^{\mathrm{vib}}$. To reveal GB atomic environments that determine the magnitude of $\Delta S_{\mathrm{GB}}^{\mathrm{vib}}$, the bond-length change of each atom (Δl) is firstly correlated with the difference in S_{μ}^{vib} between the perfect-crystal atoms and GB atoms, $\Delta S_{\mu}^{\mathrm{vib}}$, as shown in Fig. 7. One data point corresponds to the value of one atom. All atoms contained in all GB computational cells are plotted.

For MgO (Fig. 7(a)), both Mg and O ions show ~~a~~ clear positive correlations when classified into different coordination numbers, with correlation coefficients of 0.91, 0.97 and 0.97 for 4-, 5- and 6-fold coordinated atoms, respectively. This trend is consistent with our previous study [26]. Figure 7(b) shows that the Al GBs also exhibit a relatively strong correlation with a correlation coefficient of 0.78, irrespective of the coordination numbers. It is also observed that the Al GBs have a wider range of Δl and $\Delta S_{\mu}^{\mathrm{vib}}$ values than the MgO GBs. It is noted that some Mg/O atoms and Al atoms deviate from the linear relationship. This is because GB structures involve not only bond-length changes but also changes in coordination number and atomic configuration simultaneously. It is noted that simple expansion and compression of the perfect crystal merely result in phonon-mode shift toward low and high frequencies, respectively, while maintaining the overall shape of the phonon DOS. Nevertheless, the above results suggest that although MgO and Al have the dissimilar bonding nature, bond-length changes are likely to be critical in determining $\Delta S_{\mu}^{\mathrm{vib}}$ and hence $\Delta S_{\mathrm{GB}}^{\mathrm{vib}}$ for these substances.

In contrast, the Si GBs show a somewhat complex correlation between Δl and $\Delta S_{\mu}^{\mathrm{vib}}$, as shown in Fig. 7(c). Most of Si atoms with 4-fold coordination appear to follow a linear relationship with a correlation coefficient of 0.81, the 3-fold coordinated atoms clearly deviate from the correlation followed by 4-fold coordinated atoms. This trend is different from those of the MgO and Al GBs (Figs. 7(a) and 7(b)). The deviation observed for the Si GBs may indicate the importance of another factor to be considered.

To further investigate factors in determining $\Delta S_{\mu}^{\mathrm{vib}}$ at the electronic level, crystal orbital Hamilton population (COHP) analyses implemented in the LOBSTER code [50] are applied to the Si GBs. COHP values arise from overlaps of atomic orbitals between adjacent atoms, and thus a larger value of integrated projected COHP (IpCOHP) means stronger covalency between Si atoms at the GBs. Here -IpCOHP values of Si atoms are correlated to $\Delta S_{\mu}^{\mathrm{vib}}$ as shown in Fig. 8. Although some data points deviate from a simple linear relationship, there is a negative correlation between -IpCOHP and $\Delta S_{\mu}^{\mathrm{vib}}$ values. In addition, a serious deviation is absent unlike the correlation between Δl and $\Delta S_{\mu}^{\mathrm{vib}}$ (Fig. 7(c)). IpCOHP values, which directly reflect the strength of covalent bonding, may thus be a critical factor in determining excess vibrational entropies for Si GBs.

According to Eq. (4), phonon-mode shifts toward low frequencies cause~~s~~ S_{μ}^{vib} to increase. Figure 9 shows phonon PDOS profiles for atoms with positive or negative Δl values at the Σ13 GB cores. Their correlations between Δl and $\Delta S_{\mu}^{\mathrm{vib}}$ are indicated by the yellow diamonds in Fig. 7. For the Σ13(320) GB in MgO (Fig. 9(a)), the bulk Mg and O atoms have strong peaks at 8.47 THz and 11.95 THz, respectively, while these peaks become weak for the GB ions labeled as Mg1 and Mg2. Instead, new peaks appear as indicated by the black arrows. The Mg1 atom with positive Δl exhibits a lower-frequency peak at 6.92 THz, whereas the Mg2 atom with small negative Δl shows a higher-frequency peak at 18,93 THz. Similarly, the O1 and O2 atoms with positive and negative Δl show peaks at 9.50 THz and 20.22 THz, respectively.

For the Σ13(510) GB in Al (Fig. 9(b)), although the atoms at the GB also show a similar trend to those of the MgO GB, the phonon-mode shifts are more significant. The bulk Al atom originally has two peaks at 5.78 THz and 9.10 THz. For the Al1 atoms, not only these two peaks shift toward low frequencies, but also a clear low-frequency peak appears at 1.95 THz. For the Al2 atom, on the other hand, two close peaks appear at 10.23 THz and 10.78 THz in addition to ~~the~~ disappearance of the two bulk peaks. Similarly, for the Σ13(510) GB in Si (Fig. 9(c)), the Si1 atom with positive Δl shows disappearance of the strong bulk peak at 14.28 THz.

The above results indicate that for all three substances, bond length changes of GB atoms are closely related to phonon-mode shifts toward high and low frequencies. In addition, the above results imply that if a GB contains many GB atoms with longer bond lengths than the bulk value, it is expected to have a large positive value of $\Delta S_{\mathrm{GB}}^{\mathrm{vib}}$. Thus crystallographically more complicated GBs, such as asymmetric, mixed GBs and triple junctions, may contain many such atoms and exhibit large excess vibrational entropies.

3.5 Comparison between DFT calculations and empirical interatomic potentials

In this final section, DFT calculations and empirical interatomic potentials commonly used are compared with respect to excess thermodynamic and vibrational properties, in order to investigate the applicability of empirical potentials to GB thermodynamics. Figure 10 shows their correlations of $\Delta E_{\mathrm{GB}}^{\mathrm{static}}$ (zero-temperature GB energies as defined in Sec. 2). Respective interatomic potentials tuned for these substances are found to reasonably well predict $\Delta E_{\mathrm{GB}}^{\mathrm{static}}$ obtained from DFT calculations, although DFT $\Delta E_{\mathrm{GB}}^{\mathrm{static}}$ values for MgO and Si are often overestimated. Nevertheless, the order of $\Delta E_{\mathrm{GB}}^{\mathrm{static}}$ obtained from DFT calculations is still well predicted by the interatomic potentials. Thus qualitative prediction of $\Delta E_{\mathrm{GB}}^{\mathrm{static}}$ would be possible by means of empirical interatomic potentials, at least for $[001]$ and $[\bar{1}10]$ STGBs.

However, this is not the case for $\Delta S_{\mathrm{GB}}^{\mathrm{vib}}$ as shown in Fig. 11. For MgO (Fig. 11(a)), the Buckingham-type potential underestimates the DFT $\Delta S_{\mathrm{GB}}^{\mathrm{vib}}$ values, and it also fails to predict the order of the DFT values. It is therefore difficult to apply the ionic interatomic potential to quantitative evaluation of $\Delta S_{\mathrm{GB}}^{\mathrm{vib}}$ even for $[001]$ and $[\bar{1}10]$ STGBs, which are the simplest GBs with respect to crystallography and atomic structures. For Al (Fig. 11(b)), the DFT and MEAM values show a positive correlation, indicating that the MEAM potential can qualitatively predict DFT $\Delta S_{\mathrm{GB}}^{\mathrm{vib}}$. However, as indicated by the blue and red arrows, some $\Delta S_{\mathrm{GB}}^{\mathrm{vib}}$ values deviate from the diagonal line and are underestimated or overestimated, depending on each GB. This suggests that the accuracy of the MEAM potential depends on individual GBs, and thus without DFT results, there would be always uncertainty about comparing MEAM $\Delta S_{\mathrm{GB}}^{\mathrm{vib}}$ values of different GBs. These results demonstrate that although the MEAM potential accurately predicts $\Delta E_{\mathrm{GB}}^{\mathrm{static}}$, its accuracy is not necessarily ensured in calculating $\Delta S_{\mathrm{GB}}^{\mathrm{vib}}$. For Si (Fig. 11(c)), although the Tersoff potential tends to overestimate DFT $\Delta S_{\mathrm{GB}}^{\mathrm{vib}}$ values, it still qualitatively predicts the order of the DFT values. It is however noted that the current work examines only $[001]$ and $[\bar{1}10]$ STGBs with low Σ values, which are relatively low-energy GBs with simple atomic structures. The accuracy of the Tersoff potential will thus need to be examined for more complex GBs.

Figure 12 shows the correlation of $\Delta S_{\mu}^{\mathrm{vib}}$, the atom-projected excess vibrational entropies. For MgO (Fig. 12(a)), the Buckingham-type potential tends to slightly underestimate DFT $\Delta S_{\mu}^{\mathrm{vib}}$ values. This corresponds to the trend in $\Delta S_{\mathrm{GB}}^{\mathrm{vib}}$ as shown in Fig. 11(a). Again, this suggests that excess vibrational entropies are difficult to quantitatively determine by using this interatomic potential. For Al (Fig. 12(b)), data points appear to more significantly deviate from the diagonal line than those of $\Delta S_{\mathrm{GB}}^{\mathrm{vib}}$ (Fig. 11(b)), although the number of data points differs with the two figures. Even for atoms contained in the same GB, both underestimation and overestimation occur depending on each atom. This indicates that errors of MEAM $\Delta S_{\mu}^{\mathrm{vib}}$ values are cancelled out, and as a result, $\Delta S_{\mathrm{GB}}^{\mathrm{vib}}$ shows the relatively well correlation between DFT and interatomic-potential values (Fig. 11(b)). However, in order to reveal the connection between GB atomic environment and excess vibrational entropy, errors of $\Delta S_{\mu}^{\mathrm{vib}}$ would be non-negligible. For Si (Fig. 12(c)), the data points encircled by dashed red and blue circles correspond to Si atoms with threefold and fivefold coordination, respectively. Using the Thereof potential, $\Delta S_{\mu}^{\mathrm{vib}}$ of the threefold-coordinated atoms are greatly overestimated whereas $\Delta S_{\mu}^{\mathrm{vib}}$ of the fivefold-coordinated atoms are underestimated. The reason that the relatively well correlation of $\Delta S_{\mathrm{GB}}^{\mathrm{vib}}$ (Fig. 11(c)) despite the large errors is that these atoms coexist at the Σ3(112) GB and ultimately the errors are cancelled out, as is shown in Al GBs.

Finally, Fig. 13 shows comparisons between the PDOS calculated from DFT and the MEAM potential. For the bulk Al atom (Fig. 13(a)), the MEAM potential qualitatively reproduce the main peak positions of DFT PDOS although it fails to reproduce the two peak intensities at 5.79 THz and 8.97 THz. In Fig. 13 (b), one GB Al atom in the Σ13(510) GB (indicated by the red arrow in Fig. 12(b)) is chosen as an example, as the atom shows the large error in $\Delta S_{\mu}^{\mathrm{vib}}$ as indicated by Fig. 12(b). For DFT calculations, there are three strong peaks at 0.89 THz, 3.88 THz and 5.91 THz. The MEAM potential also shows similar peaks, but their high-frequencies are slightly different from the DFT peak. This difference in PDOS for bulk and GB atoms ultimately leads to the error shown in Fig. 12 (b). This comparison suggests that even for Al, one of the simplest crystal systems, accurate prediction of phonon frequency modes of GB atoms is difficult to attain by using the MEAM potential.

4. Conclusion

First-principles lattice dynamics is applied to GBs in order to reveal a physical origin of excess vibrational entropies ($\Delta S_{\mathrm{GB}}^{\mathrm{vib}}$) in GB free energies ($\Delta F_{\mathrm{GB}}$) at the atomic level. Here STGBs in MgO, Al and Si were systematically compared, with consideration of both the lowest-energy and metastable structures. It was found that Al GBs tend to have larger $\Delta S_{\mathrm{GB}}^{\mathrm{vib}}$ and hence larger temperature dependence of ΔF_{GB} than MgO and Si GBs. Si GBs entirely showed less temperature dependence of ΔF_{GB} due to small $\Delta S_{\mathrm{GB}}^{\mathrm{vib}}$. Analyses of local atomic environments at GBs indicated that bond-length changes are well correlated with atom-projected vibrational entropies ($\Delta S_{\mu}^{\mathrm{vib}}$), particularly for the MgO and Al GBs. GB atoms with longer bond lengths cause their phonon PDOS to shift toward low frequencies. This trend is observed for the three substances studied, despite their difference in bonding nature. Although the current work examined the only simple crystal structures, it is expected that the same mechanism is also critical in determining excess vibrational entropies at GBs even for other more complex substances. For Si GBs, atoms with 3-fold coordination significantly deviate from the linear relationship between bond length change and $\Delta S_{\mu}^{\mathrm{vib}}$. IpCOHP values, which is a measure of covalency, showed a positive correlation to $\Delta S_{\mu}^{\mathrm{vib}}$.

Furthermore, comparisons between DFT calculation and empirical interatomic potentials are made in order to reveal their applicability to excess vibrational entropies at GBs. Their accuracy was found to depend on each substance and GB. It was also found that atom projected vibrational entropies of GB atoms involve non-negligible errors, depending on GB atoms. Such errors may be more significant for crystallographically more complex substances and GBs. Therefore, quantitative determination of GB thermodynamic properties is likely to be difficult by means of standard empirical interatomic potentials.

Acknowledgement

This work was supported by JSPS KAKENHI (Grant Number JP19H05786) and JST-CREST (Grant Number JPMJCR17J1).

References

[1] D. W. Readey and R. E. Jech, Energies and grooving kinetics of [001] tilt boundaries in nickel oxide, J. Am. Ceram. Soc. **51** (1968) 201-208.

[2] Temperature dependence of the energy of Cu [110] symmetric tilt grain boundaries, J. Mater. Sci. Lett. **13** (1994) 46-48.

[3] T. Tsoga, P. Nikolopoulos, Surface and grain-boundary energies in yttria-stabilized ziroconia, (YSZ-8 mol%), J. Mater. Sci. **31** (1996) 5409-5413.

[4] M.N. Kelly, S.A. Bojarski, G.S. Rohrer, The temperature dependence of the relative grain-boundary energy of yttria-doped alumina, J. Am. Ceram. Soc. **100** (2017) 783-791.

[5] D. Wolf, Structure-energy correlation for grain boundaries in F.C.C. metals—Ⅲ. Symmetrical tilt boundaries, Acta Metall. Mater. **38** (1990) 781-790.

[6] D.L. Olmsted, S.M. Foiles, E.A. Holm, Survey of computed grain boundary properties in face-centered cubic metals: Ⅰ. Grain boundary energy, Acta Mater. **57** (2009) 3694-3703.

[7] J. Zhang, C.-Z. Wang, K.-M. Ho, Finding the low-energy structures of Si[001] symmetric tilt grain boundaries with a genetic algorithm, Phys. Rev. B **80** (2009) 17402.

[8] L. Wang, W. Yu, S. Shen, Revisiting the structures and energies of silicon <110> symmetric tilt grain boundaries, J. Mater. Res. **34** (2019) 1021-1033.

[9] J.H. Harding, D.J. Harris, Computer simulation of general grain boundaries in rocksalt oxides, Phys. Rev. B **60** (1999) 2740-2746.

[10] T. Yokoi, M. Yoshiya, “Atomistic simulations of grain boundary transformation under high pressures in MgO”, Physica B: Condens. Matter. **532** (2018) 2-8.

[11] S. Fujii, T. Yokoi, M. Yoshiya, Atomistic mechanisms of thermal transport across symmetric tilt grain boundaries in MgO, Acta Mater. **171** (2019) 154-162.

[12] J. Han, V. Vitek, D.J. Srolovitz, Grain-boundary metastability and its statistical properties, Acta Mater. **104** (2016) 259-273.

[13] T. Frolov, W. Setyawan, R.J. Kurtz, J. Marian, A.R. Oganov, R.E. Rudd, Q. Zhu, Grain boundary phases in bcc metals, Nanoscale **10** (2018) 8253-8268.

[14] S.J. Dillon, M.P. Harmer, Multiple grain boundary transition in ceramics: A case study of alumina, Acta Mater. **55** (2007) 5247-5254.

[15] S.V. Divinski, H. Edelhoff, Diffusion and segregation of silver in copper Σ5(310) grain boundary, Phys. Rev. B **85** (2012) 144104.

[16] T. Meiners, T. Frolov, R.E. Rudd, G. Dehm, C.H. Liebscher, Observations of grain-boundary phase transformations in an elemental metal, Nature **579** (2020) 375-378.

[17] M. Hashimoto, Y. Ishida, R. Yamamoto, M. Doyama, Thermodynamic properties of coincidence boundaries in aluminum, Acta Metal. **29** (1981) 617-626.

[18] R. Najafabadi, D. J. Srolovitz, and R. LeSar, Thermodynamic and structural properties of [001] twist boundaries in gold, J. Mater. Res. **6** (1991) 999-1011.

[19] A. Hairie, F. Hairie, B. Lebouvier, G. Nouet, E. Paumier, N. Ralantoson, and A. P. Sutton, Free energies of interfaces from quasi-harmonic theory: a critical appraisal, Interface Sci. **2** (1994) 17-29.

[20] D. J. Harris, G. W. Watson, and S. C. Parker, Atomistic simulation of the effect of temperature and pressure on the [001] symmetric tilt grain boundaries of MgO, Philos. Mag. A **74** (1996) 407-418.

[21] N.A. Benedek, A.L.-S. Chua, C. Elsässer, A.P. Sutton, M.W. Finnis, Interatomic potential for strontium titanate: An assessment of their transferability and comparison with density functional theory, Phys. Rev. B **78** (2008) 064110.

[22] D. Scheiber, R. Pippan, P. Puschnig, L. Romaner, Ab initio calculations of grain boundaries in bcc metals, Modelling Simul. Mater. Sci. Eng. **24** (2016) 035013.

[23] S. Starikov, M. Mrovec, R. Drautz, Study of grain boundary self-diffusion in iron with different atomistic models, Acta Mater. **188** (2020) 560-569.

[24] D. Scheiber, O. Renk, M. Popov, L. Romaner, Temperature dependence of surface and grain boundary energies from first principles, Phys. Rev. B **101** (2020) 174103.

[25] T. Cheng, D. Fang, Y. Yang, A temperature-dependent surface free energy model for solid single crystals, Appl. Surf. Sci. **393** (2017) 364-368.

[26] T. Yokoi, Y. Arakawa, K. Ikawa, A. Nakamura, K. Matsunaga, Dependence of excess vibrational entropies on grain boundary structures in MgO: a first-principles lattice dynamics, Phys. Rev. Mater. **4** (2020) 026002.

[27] P.E. Elöchl, Projector augmented-wave method, Phys. Rev. B **50** (1994) 17953-17979.

[28] G. Kresse, and D. Joubert, From ultrasoft pseudopotentials to the projector augmented-wave method, Phys. Rev. B **59** (1999) 1758-1775

[29] G. Kresse, and J. Furthmüller, Efficiency of ab-initio total energy calculations for metals and

semiconductors using a plane-wave basis set, Comput. Mater. Sci. **6** (1996) 15-50.

[30] G. Kresse, and J. Furthmüller, Efficient iterative schemes for ab initio total-energy calculations using a plane-wave basis set, Phys. Rev. B **54** (1996) 11169-11186.

[31] J.P. Perdew, A. Ruzsinszky, G.I. Csonka, O.A. Vydrov, G.E. Scuseria, L.A. Constantin, X. Zhou, K. Burke, Restoring the Density-Gradient Expansion for Exchange in Solids and Surfaces. Phys. Rev. Lett. **100** (2008) 136406.

[32] J.D. Gale, GULP: A computer program for the symmetry-adapted simulation of solids, J. Chem. Soc., Faraday Trans. **93(4)** (1997) 629-637.

[33] F. Landuzzi, L Pasquini, S. Giusepponi, M. Celino, A. Montone, P.L. Palla, F. Cleri, Molecular dynamics of ionic self-diffusion at an MgO grain boundary, J. Mater. Sci. **50** (2015) 2502-2509.

[34] J. Tersoff, Empirical interatomic potential for silicon with improved elastic properties, Phys. Rev. B **38** (1988) 9902-9905.

[35] B.-J. Lee, J.-H. Shim, M.I. Baskes, Semiempirical atomic potentials for the fcc metals Cu, Ag, Au, Ni, Pd, Pt, Al and Pb based on first and second nearest-neighbor modified embedded atom method, Phys. Rev. B **68** (2003) 144112.

[36] A. Togo, I. Tanaka, Frist principles phonon calculations in materials science, Scr. Mater. **108** (2015) 1-5.

[37] R. Freitas, R.E. Rudd, M. Asta, T. Frolov, Free energy of grain boundary phases: Atomistic calculations for Σ5(310)[001] grain boundary in Cu, Phys. Rev. Mater. 2 (2018) 093603.

[38] K.P. McKenna, A.L. Shluger, First-principles calculations of defects near a grain boundary in MgO, Phys. Rev. B **79** (2009) 224116.

[39] J.J. Bean, M. Saito, S. Fukami, H. Sato, S. Ikeda, H. Ohno, Y. Ikuhara, K.P. McKenna, Atomic structure and electronic properties of MgO grain boundaries in tunneling magnetoresistive devices, Sci. Rep. **7** (2017) 45594.

[40] D.M. Duffy, P.W. Tasker, Computer simulation of <001> tilt grain boundaries in nickel oxide, Philos. Mag. A **47** (1983) 817-825.

[41] J.D. Rittner, D.N. Seidman, <110> symmetric tilt grain-boundary structures in fcc metals with low stacking-fault energies, Phys. Rev. B **54** (1996) 6999-7015.

[42] M.A. Tschopp, D.L. McDowell, Structures and energies of Σ3 asymmetric tilt grain boundaries in copper and aluminium, Philos. Mag. **87** (2007) 3147-3173.

[43] M.A. Tschopp, D.L. McDowell, Asymmetric tilt grain boundary structure and energy in copper and aluminium, Philos. Mag. **87** (2007) 3871-3892.

[44] M. Rajagopalan, M.A. Bhatia, M.A. Tschopp, D.J. Srolovitz, K.N. Solanki, Atomic-scale analysis of liquid-gallium embrittlement of aluminum grain boundaries, Acta Mater **73** (2014) 321-325.

[45] I. Adlakha, M.A. Bhatia, M.A. Tschopp, K.N. Solanki, Atomic scale investigation of grain boundary structure role on intergranular deformation in aluminium, Philos. Mag. **94** (2014) 3445-3466.

[46] B. Ziebarth, M. Mrovec, C. Elsässer, P. Gumbsch, Interstitial iron impurities at grain boundaries in silicon: A first-principles study, Phys. Rev. B **91** (2015) 035309.

[47] L. Wang, W. Yu, S. Shen, Revisiting the structures and energies of silicon <110> symmetric tilt grain boundaries, J. Mater. Res. **34** (2019) 1021-1033.

[48] J.R. Morris, Z.-Y. Lu, D.M. Ring, J.-B. Xiang, K.-M. Ho, C.Z. Wang, First-principles determination of the $\Sigma = 13$ {510} symmetric tilt boundary structure in silicon and germanium, Phys. Rev. B **58** (1998) 11241-11245.

[49] T. Yokoi, Y. Kondo, K. Ikawa, A. Nakamura, K. Matsunaga, Asymmetric tilt grain boundaries in MgO: A simulated annealing approach, J. Mater. Sci. **56** (2021) 3183-3196.

[50] S. Maintz, V.L. Deringer, A.L. Tchougréeff, R. Dronskowski, LOBSTER: A tool to extract chemical bonding from plane-wave based DFT, J. Comput. Chem. **37** (2016) 1030-1035.

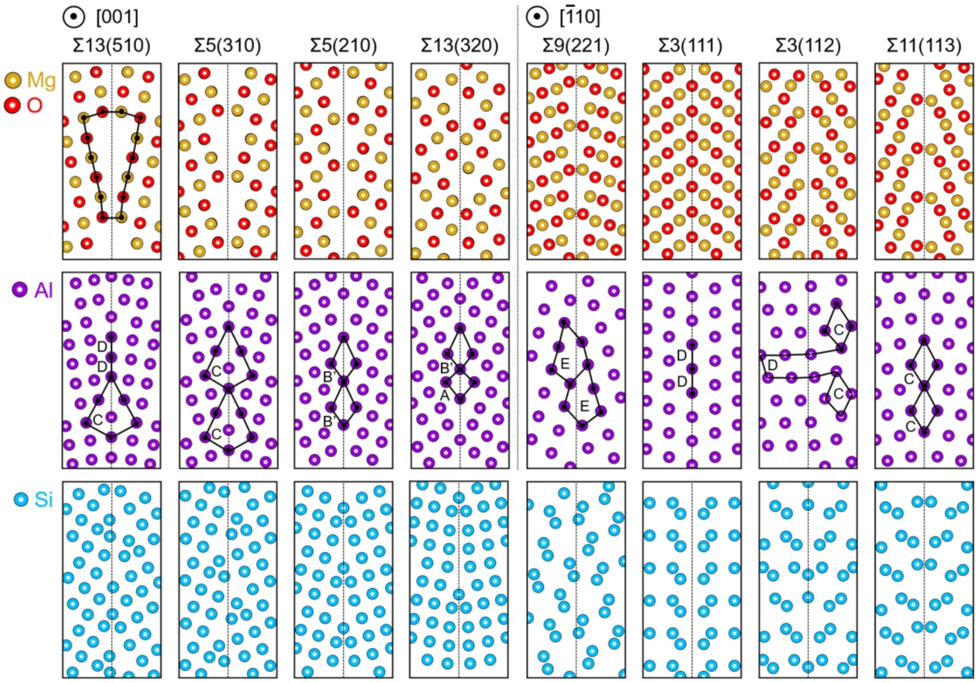

Fig. 1 Lowest-energy GB structures obtained from the γ-surface method and used for lattice dynamics calculation for MgO, Al and Si.

330x232mm (150 x 150 DPI)

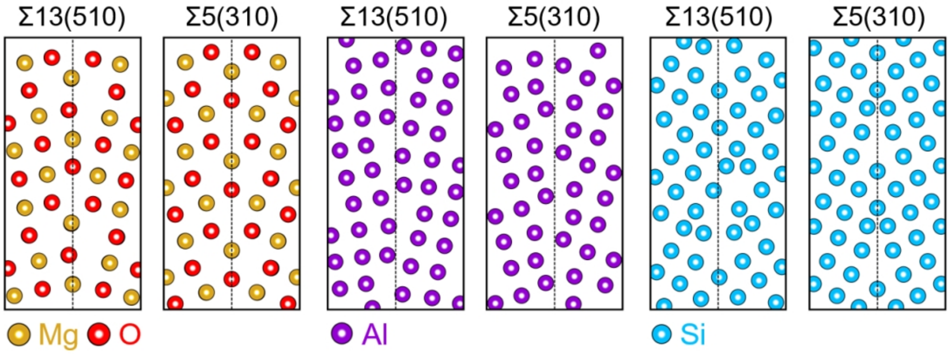

Fig. 2 Σ13(510) and Σ5(310) metastable structures viewed along the [001] axis.

238x92mm (150 x 150 DPI)

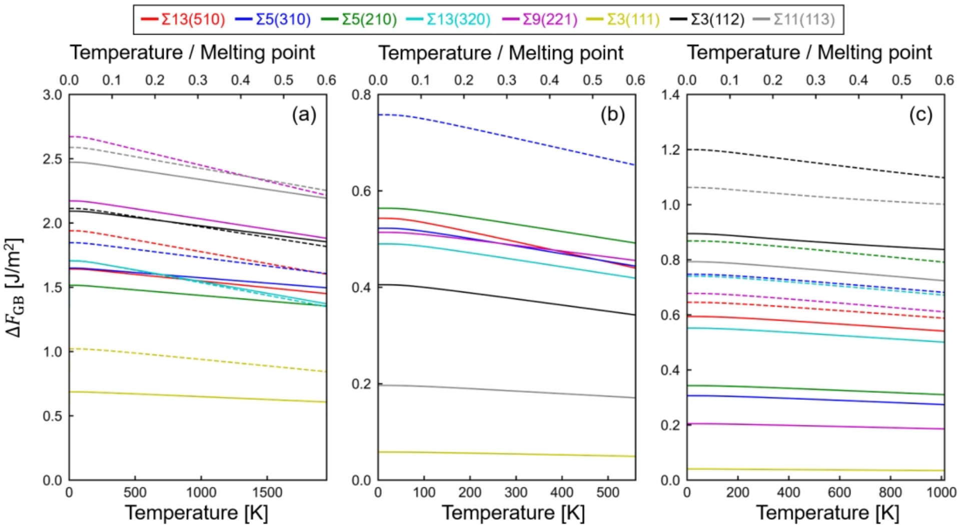

Fig. 3 GB free energies (ΔF_{GB}) as functions of temperature and the ratio of temperature to the melting points for (a) MgO, (b) Al and (c) Si. The melting temperatures are 3250 K, 933 K and 1687 K for MgO, Al and Si, respectively. Each line indicates ΔF_{GB} for the corresponding GB. The solid and dashed lines with the same color represent ΔF_{GB} of the lowest-energy and metastable structures for the same GB, respectively.

313x171mm (150 x 150 DPI)

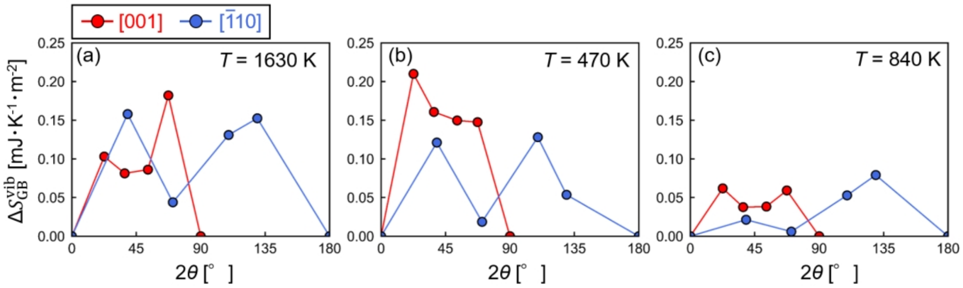

Fig. 4 Excess vibrational entropies ($\Delta S^{\mathrm{vib}}{}_{\mathrm{GB}}$) as a function of misorientation angle (2θ) for (a) MgO, (b) Al and (c) Si. The values at around half of the melting points are plotted: 1630 K for MgO, 470 K for Al and 840 K for Si.

317x98mm (150 x 150 DPI)

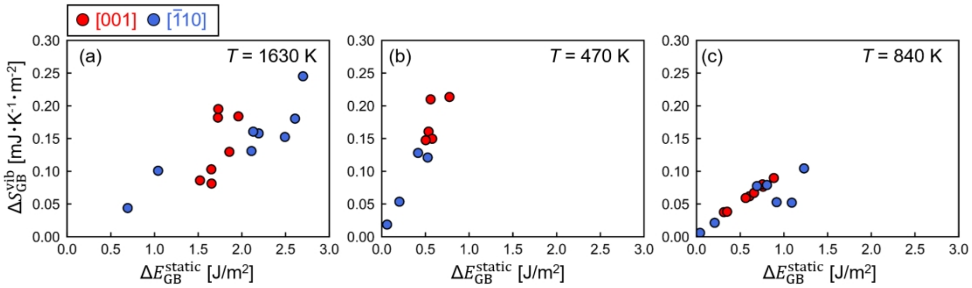

Fig. 5 Correlations between $\Delta E_{GB}{}^{static}$ and $\Delta S_{GB}{}^{vib}$ at around half of the melting points for (a) MgO, (b) Al and (c) Si. Both the lowest-energy and metastable structures are indicated.

341x105mm (150 x 150 DPI)

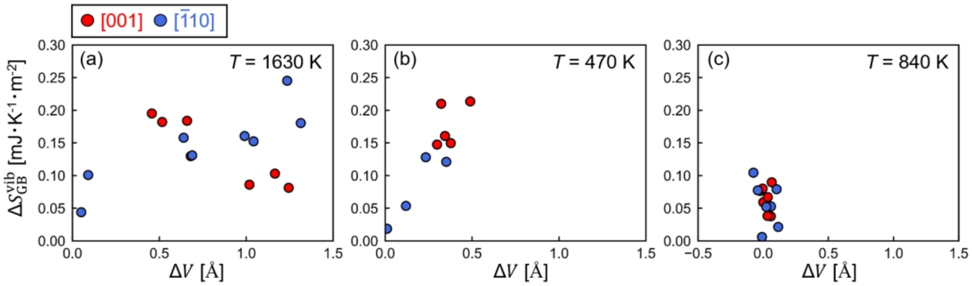

Fig. 6 Correlations between ΔV and ΔS_{GB}^{vib} at around half of the melting points for (a) MgO, (b) Al and (c) Si. Both the lowest-energy and metastable structures are indicated.

331x100mm (150 x 150 DPI)

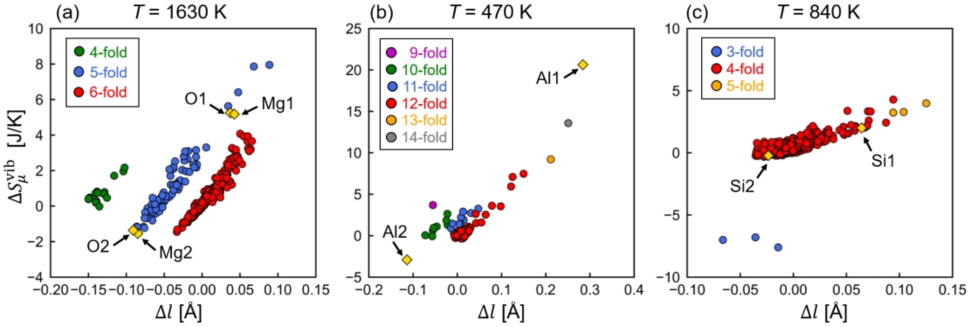

Fig. 7 Correlations between bond-length changes from the bulk value (*Δl*) and changes in atom-projected vibrational entropy from the bulk value ($\Delta S_\mu^{\mathrm{vib}}$) for (a) MgO, (b) Al and (c) Si. One data point corresponds to those for a specific atom contained in a GB computational cell. The data points are colored with respect to the coordination number of each atom. The GB atoms indicated by the yellow diamond are used to plot their phonon PDOS (see Fig. 9).

326x114mm (150 x 150 DPI)

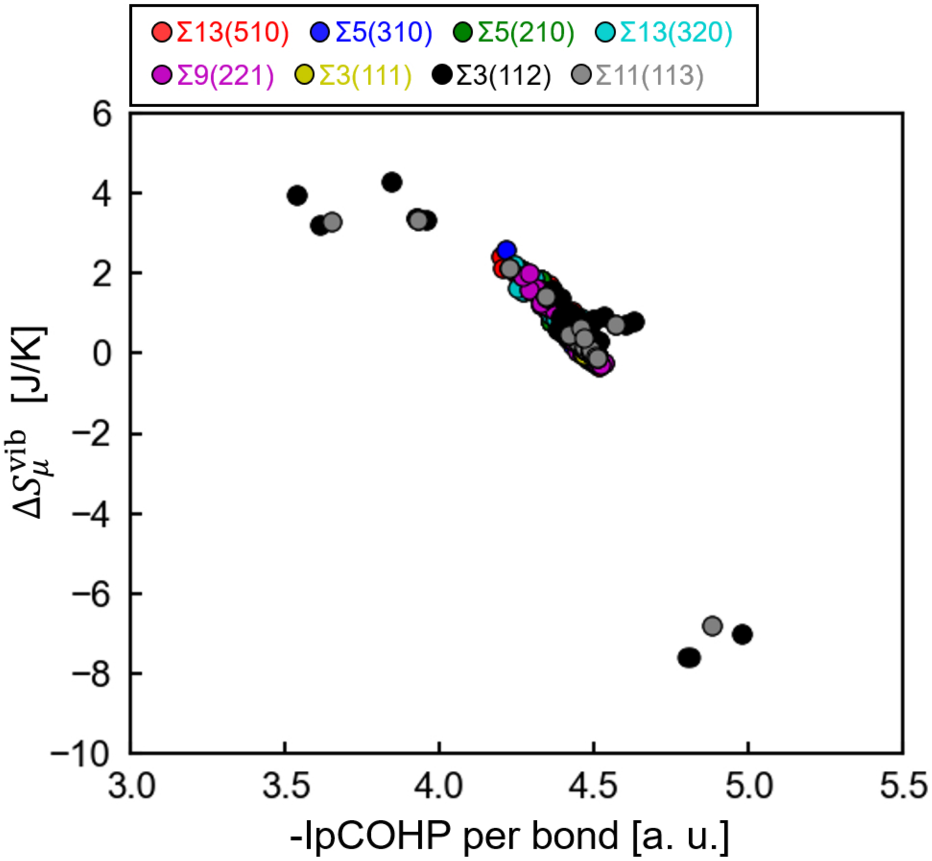

Fig. 8 Correlation between IpCOHP values and $\Delta S_{\mu}^{\mathrm{vib}}$ for each Si atom in the GBs.

176x159mm (150 x 150 DPI)

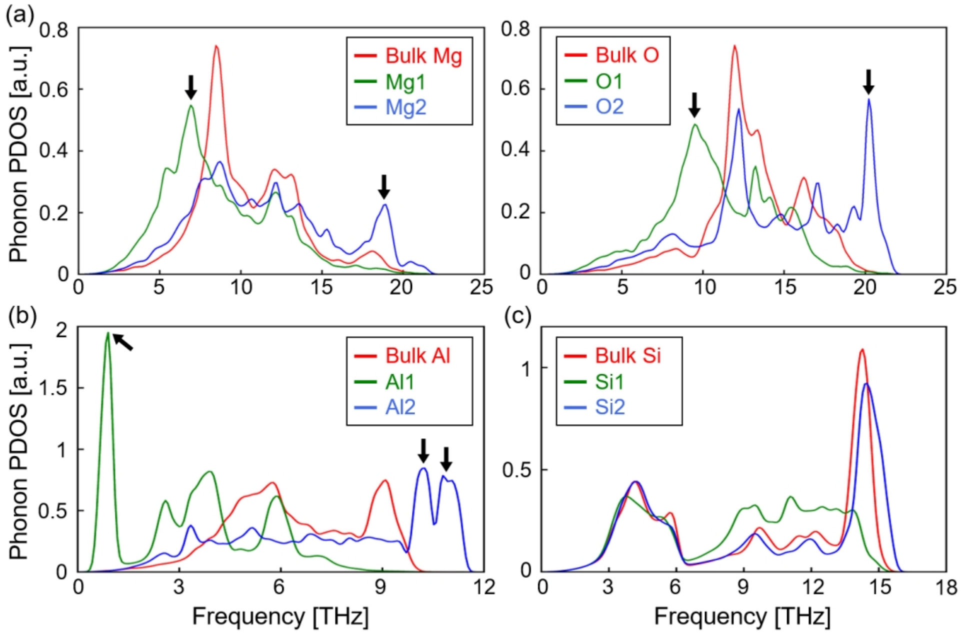

Fig. 9 Phonon PDOS curves of the GB atoms indicated by the yellow diamond in Fig. 7 for (a) the Σ13(320) GB in MgO, (b) the Σ13(510) GB in Al and (c) the Σ13(510) GB in Si. The black arrows indicate characteristic peaks observed for GB atoms.

263x177mm (150 x 150 DPI)

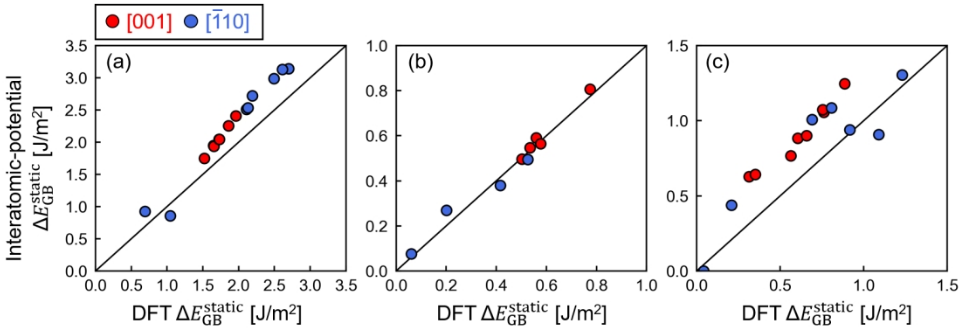

Fig. 10 Correlations between ΔE^{static}_{GB} calculated from DFT calculations and the empirical interatomic potentials for (a) MgO, (b) Al and (c) Si.

307x107mm (150 x 150 DPI)

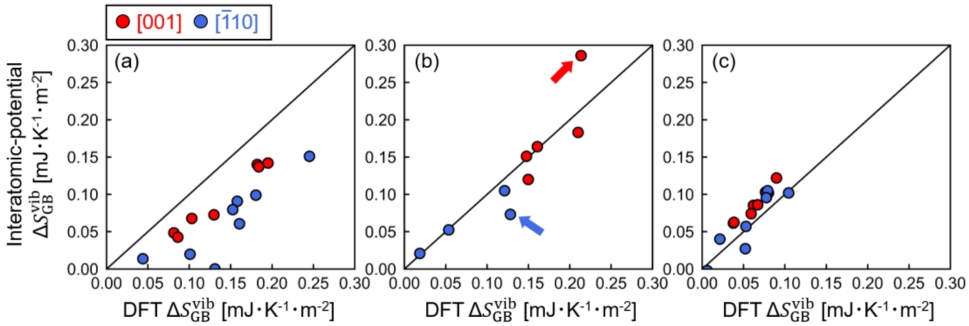

Fig. 11 Correlations between $\Delta S_{GB}{}^{vib}$ calculated from DFT calculations and the empirical interatomic potentials for (a) MgO, (b) Al and (c) Si.

310x108mm (150 x 150 DPI)

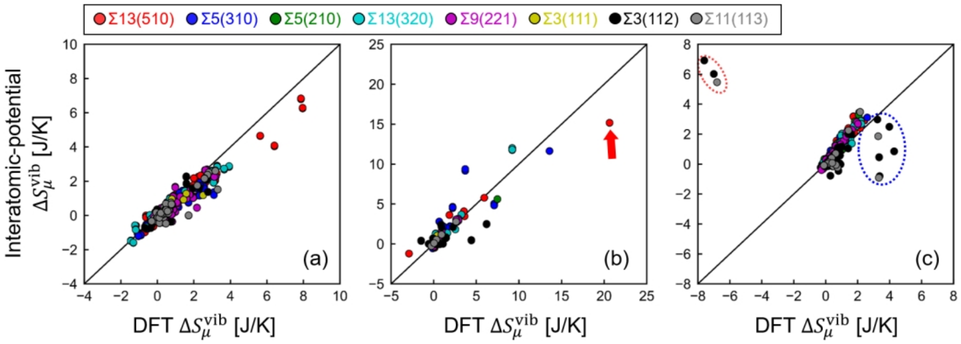

Fig. 12 Correlations between $\Delta S_{\mu}^{\mathrm{vib}}$ calculated from DFT calculations and the empirical interatomic potentials for (a) MgO, (b) Al and (c) Si.

301x113mm (150 x 150 DPI)

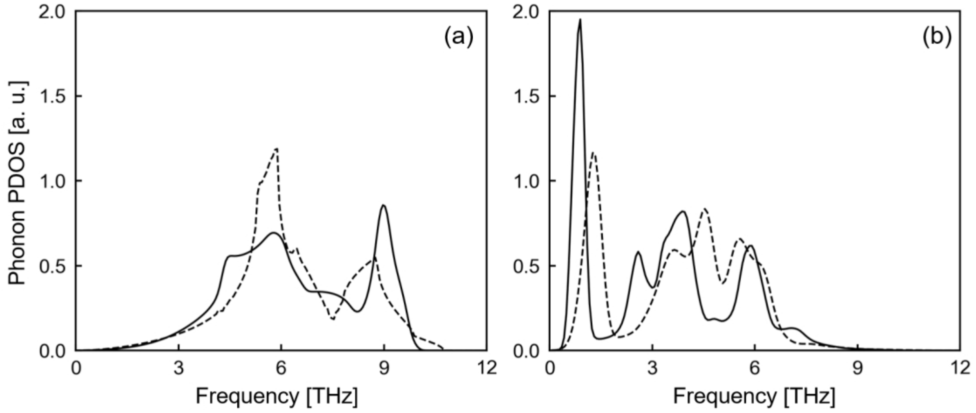

Fig. 13 Phonon partial density of states (PDOS) obtained from DFT calculations (solid line) and the MEAM potential (dashed line) for (a) the bulk Al atom and (b) a GB Al atom in the Σ13(510) GB.

287x130mm (150 x 150 DPI)

Table 1 Crystallographic properties of GBs studied. N_{cell} is the number of atoms in a simulation cell used for structural optimization, and L_x is the distance between two GB planes along the *x*-axis direction. A misorientation angle of two grains about the tilt axis is denoted as 2θ.

Σ value/GB plane/ Tilt axis	2θ [°]	N_{cell}			L_x [Å]		
		Al	Si	MgO	Al	Si	MgO
$\Sigma13(510)/[001]$	22.62	78	108	156	15.73	14.55	17.42
$\Sigma5(310)/[001]$	36.87	40	80	80	13.20	17.36	14.63
$\Sigma5(210)/[001]$	52.13	60	80	160	14.07	12.20	19.83
$\Sigma13(320)/[001]$	67.38	104	100	208	14.90	18.83	15.70
$\Sigma9(221)/[\bar{1}10]$	38.94	38	72	72	13.12	16.36	13.13
$\Sigma3(111)/[\bar{1}10]$	70.53	28	48	48	16.28	18.84	14.72
$\Sigma3(112)/[\bar{1}10]$	109.47	38	72	72	15.88	20.20	16.25
$\Sigma11(113)/[\bar{1}10]$	129.52	24	46	88	14.75	18.14	15.09